

Chapter 6

Sliding friction under normal loading variation

6.1 Introduction

The friction between macroscopic bodies involves shearing of myriads of micro-asperity contacts. The mechanical understanding of such systems starts by the study of an individual micro-asperity. Such approach is widely study under constant normal force, however, in many practical applications micro-asperities are submitted to inclined planes resulting in a variable normal loading during sliding.

In this chapter, it is proposed a simultaneous variation of the normal and the tangential loadings. For this, a slight tilt between the contact interface and the xy-plane is introduced. In this way, contributing with one more element for the understanding of a more realistic and complex system.

6.2 Experimental investigation

The experiments were carried out using the tribometer presented in Section 3.3.1 on S1R9 samples (one sphere of a radius of curvature of 9.42 mm, see Section 3.2.1) against a glass plate. Tangential loading tests with simultaneous normal loading variation were performed by introducing a slight tilt between the glass plate and the direction of the tangential loading. For this, two cases were considered:

Case A - Tilt of the plate slider: the tilt was introduced using the goniometer located above the tangential force sensor and the cantilever. That way not only the plate

is tilted, but also the cantilever and the tangential force sensors, as shown in red in Fig. 6.1. This case presents a normal attachment configuration (defined in Fig. 3.7) - sphere (in red) at the bottom and plate (in blue) at the top.

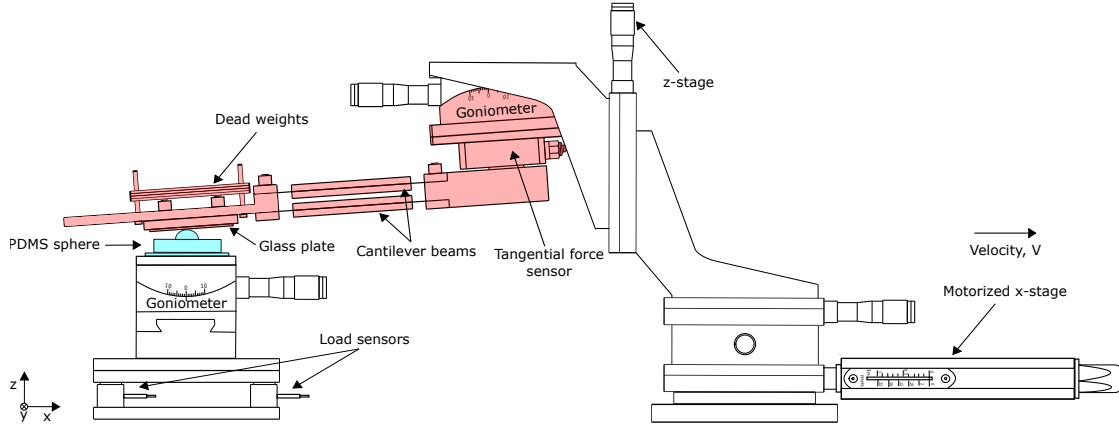


Figure 6.1: Setup of Case A - Tilt of the plate slider.

Case B - Tilt of the plate fixed: here, the goniometer located under the plate fixed was responsible for tilting, as shown in Fig. 6.2. This case presents an inverse attachment configuration (also defined in Fig. 3.7) - sphere (in blue) at the top and the plate (in red) at the bottom (as in Fig. 3.7).

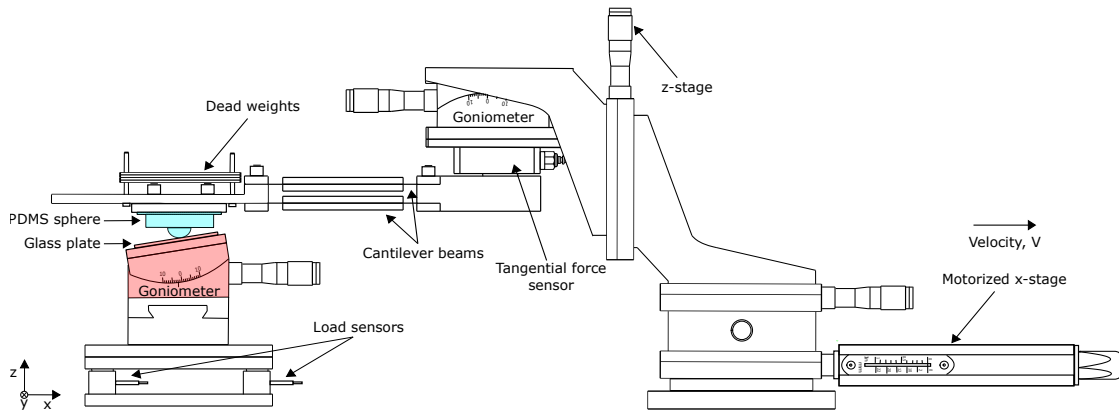


Figure 6.2: Setup of Case B - Tilt of the attached plate.

First, the normal load was applied by adding dead weights, and second, the tilt was set up using the respective goniometer for each case. After that, the normal force was verified with the normal load sensors and adjusted to achieve the target load via the z-stage, which pushes the whole cantilever on the sphere (resp. glass plate) in a normal (resp. inverse) attachment configuration. The tilt is defined by an angle ϕ between the contact interface plane and the xy-plane. When the motion of the sphere is in the

direction rising the plate is a positive angle, as shown in Fig. 6.3. The tangential force was imposed on the glass plate (on the sphere for the inverse configuration) at a constant velocity $V = 0.1 \text{ mm/s}$. Images of the contact area during the running of the tangential force were recorded. The lateral square pixel varied in the range of $7.90 \mu\text{m} - 9.06 \mu\text{m}$ between the set of experiments. **Talk about the extraction of the A from the images.** A contact area correction was made, since when there is an angle with the z-axis the camera captures a project area $A_{project} = A \cdot \cos \phi$ onto the xy-plane. Full details and specifications of the experimental procedure are given in Chapter 3.3.2.

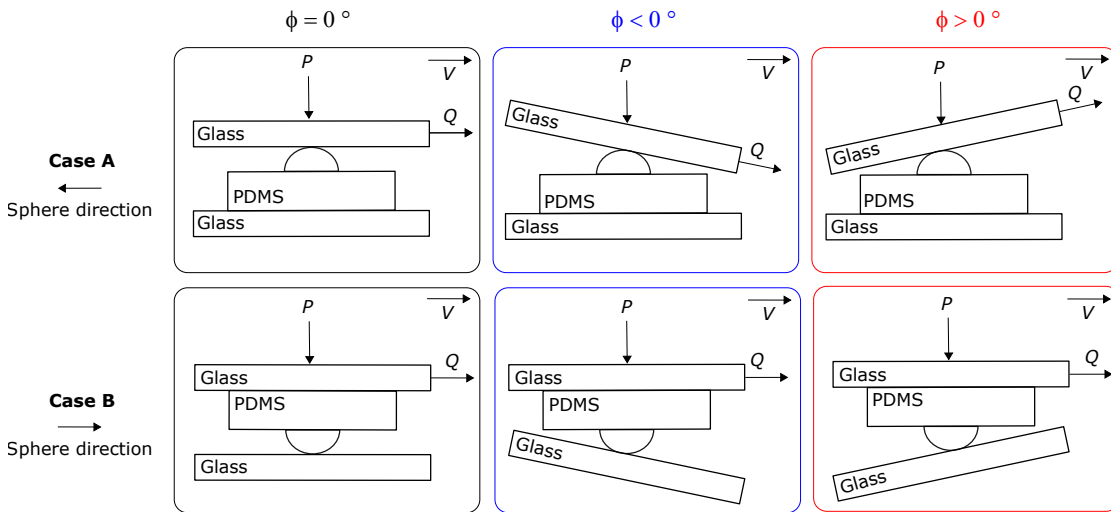


Figure 6.3: Definition of the angle of inclination, ϕ . Case A: tilt of the plate slider. Case B: tilt of the plate fixed. Left: aligned configuration ($\phi = 0$), centre: $\phi < 0$, and right: $\phi > 0$.

The sets of experiments performed are presented below:

Table 6.1: Sets of experiments.

Case	Range of ϕ	P	Sample
■ A	-4 to 4°	0.78 N	S1R9 (4)
▲ B(i)	-2.5 to 4°	0.78 N	S1R9 (4)
◆ B(ii)	-3 to 4°	0.78 N	S1R9 (5)
▼ B(iii)	-2.5 to 4°	0.10 N	S1R9 (5)
● B(iv)	-2 $^\circ$	-0.6 mN to 3.20 N	S1R9 (2)
● B(iv)	0 $^\circ$	-0.2 mN to 3.21 N	S1R9 (2)
● B(iv)	2 $^\circ$	-2.3 mN to 3.19 N	S1R9 (2)

Should I say why this forces? and spheres?

For case A, first, the aligned experiment $\phi = 0$ was carried out. Second, $\phi > 0$ in an ascending order. And last, $\phi < 0$ in a descending order. For cases B(i,ii, and iii), the experiments were performed in the following order: $\phi = 0$, $\phi < 0$ (descending

order), and $\phi > 0$ (ascending order). For case B(iv), the experiments were carried out randomly in relation to the applied normal forces, and ϕ was modified every 5 tests in the order: $\phi = 0, -2$, and 2° . For example, 5 different normal forces (randomly selected) at $\phi = 0^\circ$ were tested. Then the same 5 normal forces were tested for $\phi = -2^\circ$, and last the same 5 normal forces for $\phi = 2^\circ$. We inform that an angle ϕ less than -3° , for case B, could not be obtained because the projected contact area touches the edge of the field of view detected by the camera, so the contact area cannot be detected correctly.

6.3 Results and analysis

In this section, first will be present the results and analyses of case A (tilt of the plate slider) and second, case B (tilt of the plate fixed).

6.3.1 Case A: tilt of the plate slider

Fig. 6.4, shows the evolution of (a) the tangential force Q and (b) the normal force P during the glass displacement d . A typical tangential force-displacement curve behavior is observed in all angles Q . When the plate begins to move, Q increases linearly. Then, a small difference between the positive and negative angles can be notice during the slight slope before the curves reach them maximum Q_s . The values of Q_s are also a little different ($\approx 17\%$ for ϕ varying between -4 to 4°). After, Q decreases entering in a macroscopic sliding with a decay for $\phi < 0$ (blue curves) and a rise for $\phi > 0$ (red curves). As mentioned in Section 3.5, we found a greater tangential force at the beginning of the set of experiments, which may be due to the orientation, extension, and/or pull-out of the PDMS chains [12, 13, 21]. For this reason, the first tests are eliminated, however, they were considered here. The higher Q_s values for $\phi = 0, 0.5$, and 1° may be due to this phenomenon rather than a tilting effect. In the $P(d)$ curves, we can see an increase of the normal force P during the onset of sliding before entering a global sliding, and a variation of the normal force at Q_s more than 33% for a variation of ϕ in the range of -4 to 4° .

PS.: not considering the first 3 is 6%, considering is 17%.

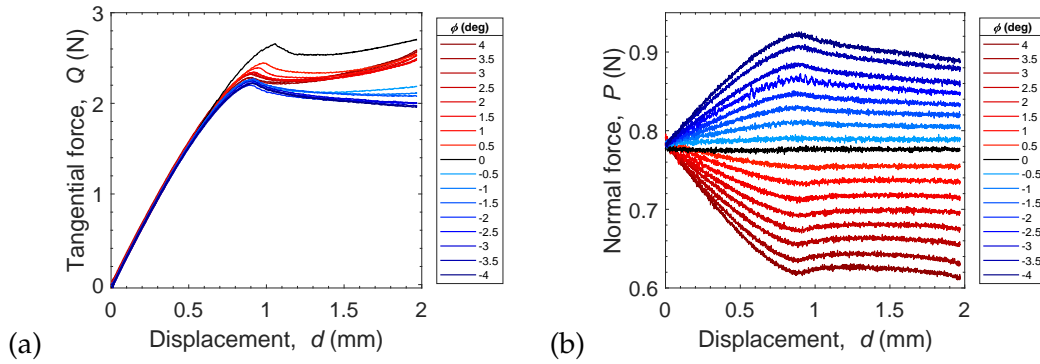


Figure 6.4: Evolution of (a) the tangential force Q and (b) the normal force P during the glass displacement d .

Fig. 6.5, shows the contact area A as a function of (a) the displacement d and (b) the tangential force Q . The tilting does not appear to have a significant effect on the reduction of A since the variation in A (up to Q_s) is less than 10%. We also see a discrepancy in the first three tests ($\phi = 0, 0.5$, and 1°), which show a greater reduction in the contact area.

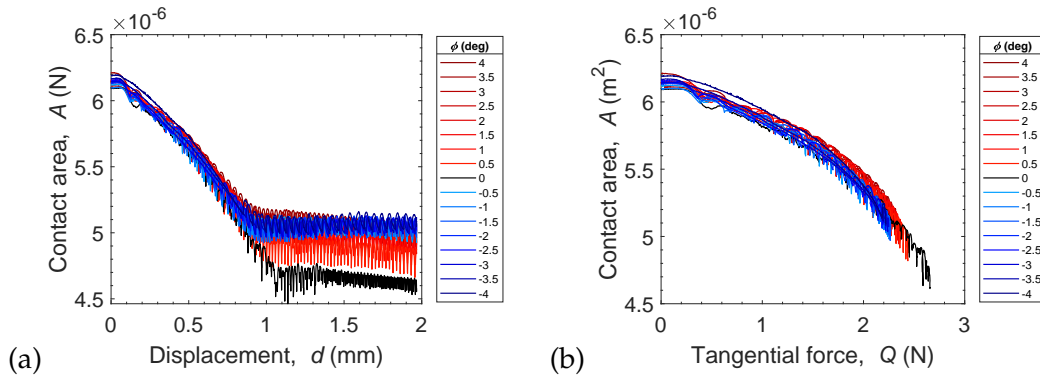


Figure 6.5: Contact area A as a function of (a) the displacement d and (b) the tangential force Q .

This non-effect of the angle variation in the results is reasonable, because the unbalanced sensor forces have been considered, which should be corrected due to the existence of the tilt, a well-known inclined plane. The forces acting upon the contact plane are shown in Fig. 6.6. There are three forces acting - the force of gravity, the normal force, and the tangential force. The force of gravity ($m.g$) acts in a downward direction, the contact normal force P_{cn} acts in a direction perpendicular to the surface, and the contact tangential force Q_{cn} parallel to the tilted surface. Thus, the sensor forces, $P = mg$ and Q_{vb} , have to be resolved into perpendicular components so they can be

added to the forces acting on the PDMS sphere. Below, the diagram in Fig. 6.6, shows how the forces (black arrows) have been replaced by their components (grey arrows).

This diagram is not correct

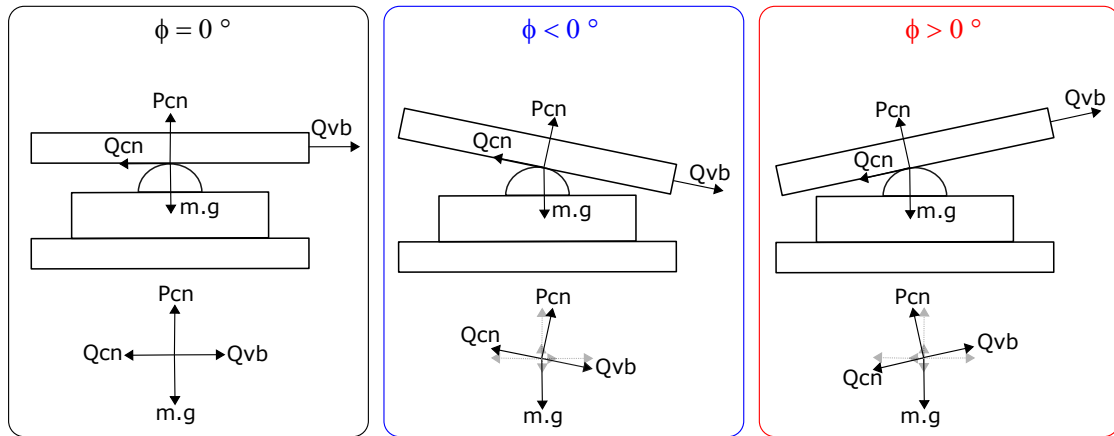


Figure 6.6: Force diagram of case A for the 3 tilt positions: $\phi = 0$, $\phi < 0$, and $\phi > 0$. Black arrows show the forces acting on the contact plane (Q_{cn} and P_{cn}) and the forces measured by the sensors ($P = m.g$ and Q_{vb}). Grey arrows represent the force components acting on the contact plane.

Then, the balanced forces acting on the contact plane are defined in the equations:

$$Q_{cn} = Q_{vb} \cdot \cos(\phi) \cdot \cos(\phi) - mg \cdot \sin(\phi) \quad (6.1)$$

$$P_{cn} = Q_{vb} \cdot \sin(\phi) \cdot \cos(\phi) + mg \cdot \cos(\phi) \quad (6.2)$$

where Q_{cn} and P_{cn} are the balanced contact tangential and normal force, respectively. Q_{vb} and mg are the tangential and normal forces measured by the sensors, respectively.

After balancing the forces, Fig. 6.7 shows the force-displacement curves of the forces acting on the contact plane, we can notice that the tilt of the plate slider, the cantilever and the tangential force sensor, proceeds in a non-variation of the normal force P received by the contact plane.

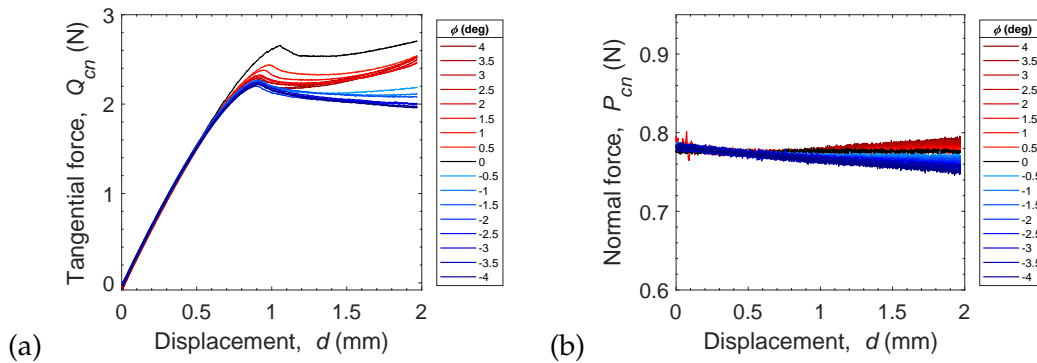


Figure 6.7: Evolution of the tangential force Q_{cn} and (b) the normal force P_{cn} during the glass displacement d .

Plot curves: alpha and sigma local before and after.

this sigma is not from the A envelope.

Should be this alpha variation due to the strong oscillations?

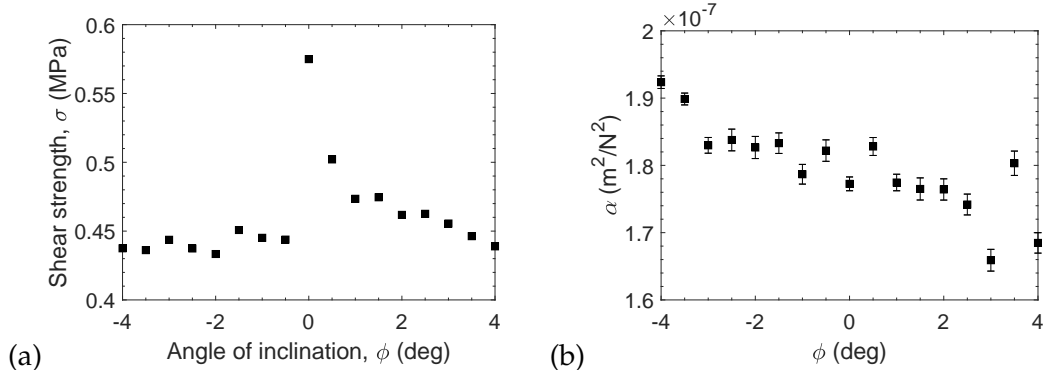


Figure 6.8: (a) Instantaneous shear strength and (b) area reduction parameter α as a function of ϕ .

6.3.2 Case B: tilt of the plate fixed

Fig. 6.9, shows the results of Case B(i), that has a initial normal force of 0.78 N and a tilt variation of -2.5 to 4°. In this figure is shown in (a) the sensor tangential force Q and in (b) the sensor normal force P as a function of the displacement d ; in (c) the contact area A evolution as a function of the displacement d and in (d) as a function of the sensor tangential force Q .

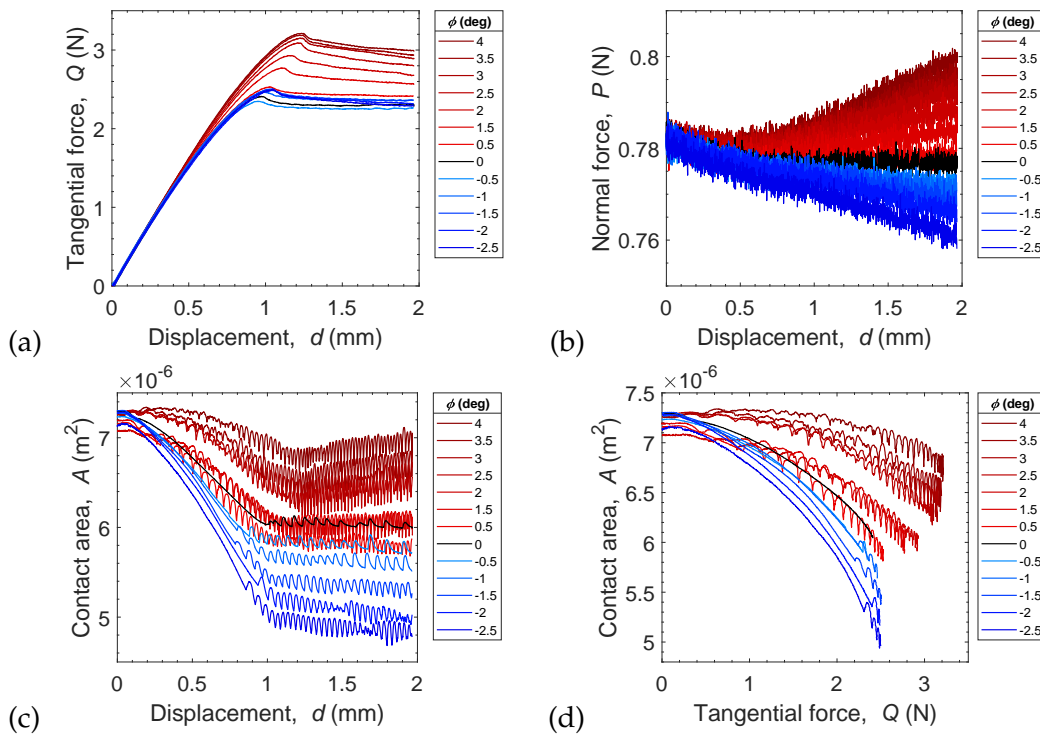


Figure 6.9: (a) The tangential force Q and (b) the normal force P as a function of the displacement d ; (c) the contact area A evolution as a function of the displacement d and (d) as a function of the tangential force Q ; for Case B(i), where the initial normal force is 0.78 N and the tilt angle ϕ range between -2.5 and 4° .

We can see that this tilt configuration gives the opposite sensor force results to Case A. And here, a variation of ϕ in the range of -2.5 to 4° results in a change in the peak of tangential force Q_s of **XX%**, while the normal force P remained constant (less than **X%**).

Thus, the unbalanced forces have been resolved to be added to the other forces acting on the PDMS sphere. Below, the diagram in Fig. 6.10, shows how the forces have been replaced by their components, following by the balanced force equations, Eq. 6.4 and 6.3.

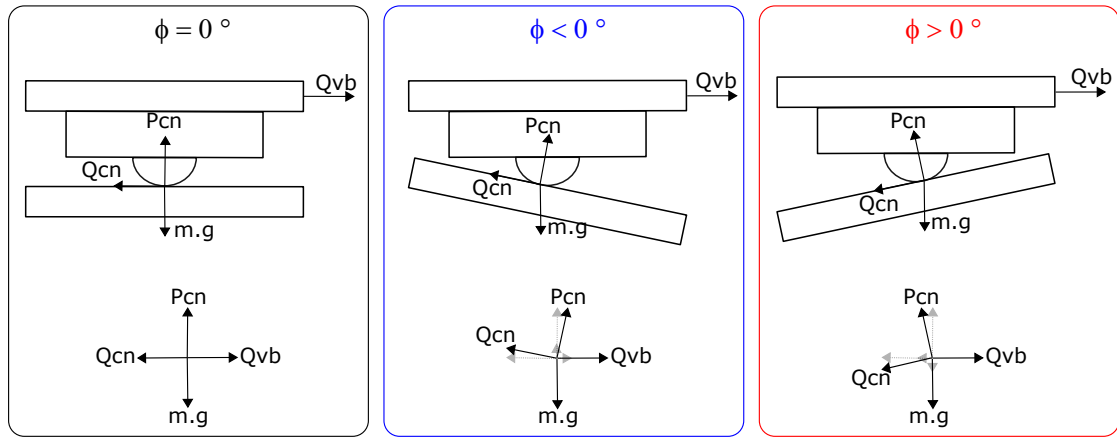


Figure 6.10: Force diagram of case B for the 3 tilt positions: $\phi = 0$, $\phi < 0$, and $\phi > 0$. Black arrows show the forces acting on the contact plane (Q_{cn} and P_{cn}) and the forces measured by the sensors ($P = m.g$ and Q_{vb}). Grey arrows represent the force components acting on the contact plane.

In equilibrium,

$$P + Q + P_{cn} + Q_{cn} = 0$$

Replacing the forces by their components,

$$P = (P_x, P_y) = (-mg \cdot \sin\phi, -mg \cdot \cos\phi)$$

$$Q = (Q_x, Q_y) = (Q \cdot \cos\phi, Q \cdot \sin\phi)$$

$$P_{cn} = (0, P_{cny}) = (0, P_{cn})$$

$$Q_{cn} = (Q_{cnx}, 0) = (Q_{cn}, 0)$$

Sum of x components:

$$-mg \cdot \sin\phi + Q \cdot \cos\phi + 0 - Q_{cn} = 0$$

which may be rewritten as

$$Q_{cn} = -mg \cdot \sin(\phi) + Q \cdot \cos(\phi) \quad (6.3)$$

Sum of y components:

$$-mg \cdot \cos\phi - Q \cdot \sin\phi + P_{cn} + 0 = 0$$

rewritten as

$$P_{cn} = mg \cdot \cos(\phi) + Q \cdot \sin(\phi) \quad (6.4)$$

After making the necessary corrections, Fig. 6.11 shows the balanced forces acting on the contact plane for the cases B(i,ii,ii, and iv). On left side is shown the tangential force Q_{cn} and on the right side the normal force P_{cn} .

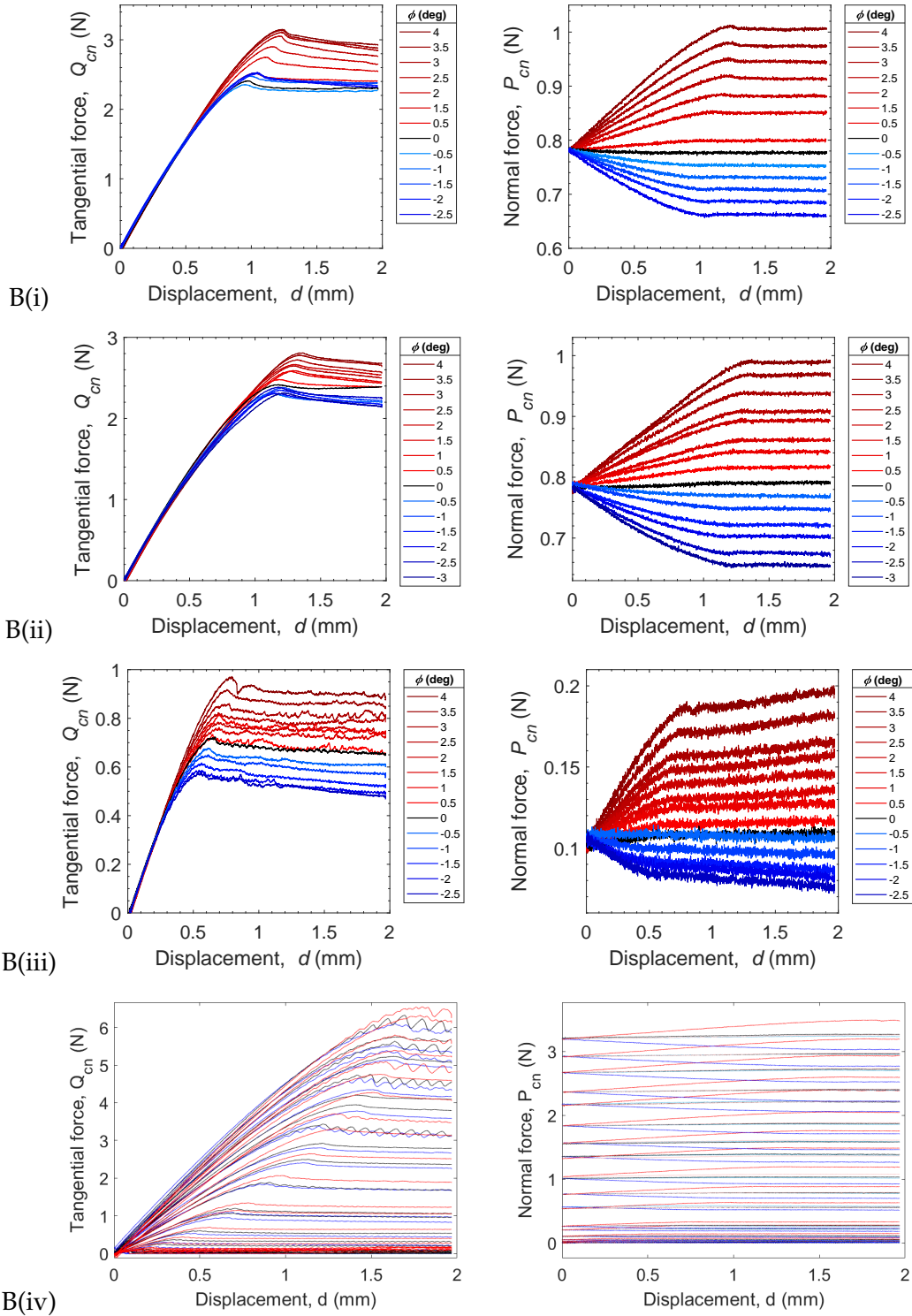


Figure 6.11: Evolution of the tangential force Q_{cn} (on the left side) and the normal force P_{cn} (on the right side) as function of the displacement d . B(i): $P = 0.78 \text{ N}$; B(ii): $P = 0.78 \text{ N}$; B(iii): $P = 0.1 \text{ N}$; B(iv): wide range of P for 3 different tilt angles (-2° : blue lines, 0° : black lines, and 2° : red lines). The color gradients for cases B(iv) are in function of the normal force P ; light colors for small P and dark colors for large P .

Fig.6.11 shows that the tilt angle ϕ significantly affects the normal force acting on the contact plane. As we can see, P_{cns} varies significantly during the onset of shearing,

which explaining the variation in the contact tangential force peak. The changes in Q_{cns} are correlated with changes in the P_{cns} , by approximately the same fraction.

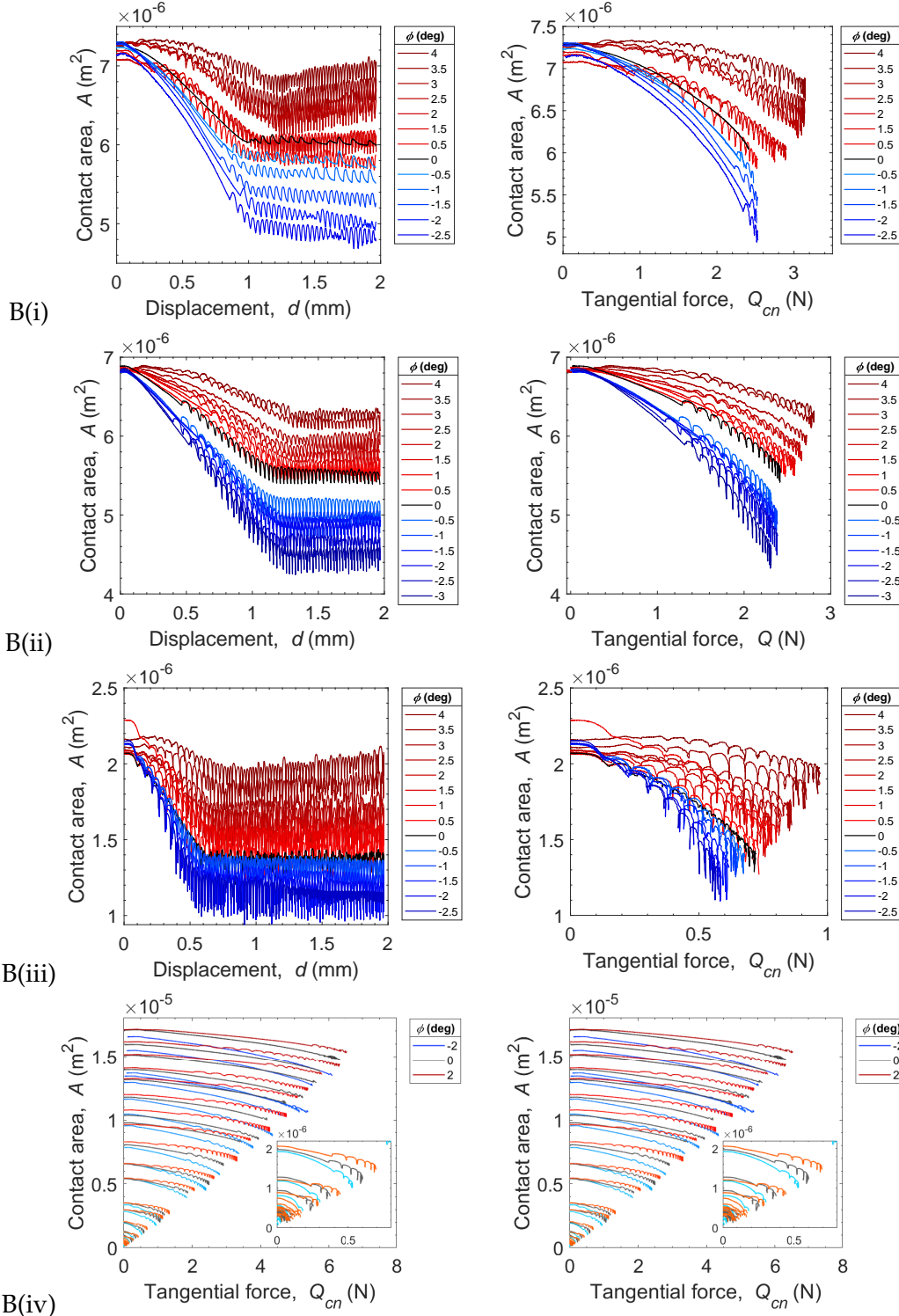


Figure 6.12: Contact area A as a function of the displacement d (on the left side) and of the tangential force Q_{cn} (on the right side). B(i): $P = 0.78$ N; B(ii): $P = 0.78$ N; B(iii): $P = 0.1$ N; B(iv): wide range of P for 3 different tilt angles (-2°: blue lines, 0°: black lines, and 2°: red lines). The color gradients for cases B(iv) are in function of the normal force P ; light colors for small P and dark colors for large P .

Table 6.2: Summary of cases B

Variation	(i)	(ii)	(iii)	(iv)
Qcn_s	$\approx 30\%$	$\approx 50\%$	$\approx 20\%$	
Pcn_s	$\approx 25\%$	$\approx 55\%$	$\approx 35\%$	
A_s	$\approx 30\%$	$\approx 40\%$	$\approx 40\%$	

The contact area reduction in shearing experiments under constant normal force has a circular initial contact area that is reduced during shearing and is accompanied by a modification of the contact area morphology, evolving from a circular form to a prolate one. Here, as we can see from Fig. 6.12(b), the ...

To verify the influence of the tilt angle ϕ on the contact area decay during the onset of shearing, the quadratic-law equation $A = A_0 - \alpha_A Q_{cn}^2$ [37], where A_0 is the contact area at zero tangential load $Q_{cn} = 0$ and α_A is a fitting area reduction parameter, were used to fit all cases B. The results are shown in Fig. 6.13, where α_A is plotted as a function of A_0 in (a) and as a function of ϕ in (b).

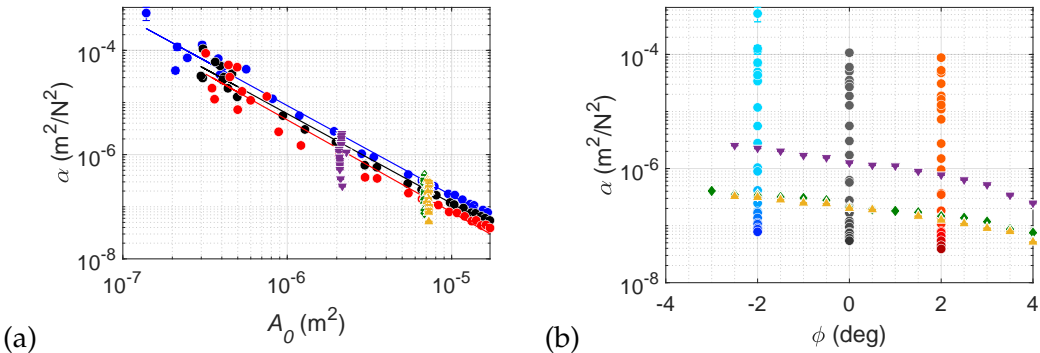


Figure 6.13: (a) Area reduction parameter α_A as a function of the initial contact area A_0 and (b) as a function of the tilt angle ϕ . \blacktriangle B(i): 0.78 N; \blacklozenge B(ii): 0.78 N; \blacktriangledown B(iii): 0.10 N; and a wide range of P for \bullet B(iv): $\phi = -2^\circ$, \bullet B(iv): $\phi = 0^\circ$, and \bullet B(iv): $\phi = 2^\circ$. The color gradients for cases B(iv) are in function of the normal force P ; light colors for small P and dark colors for large P .

The contact area decay is slightly greater for $\phi < 0$ and lower for $\phi > 0$, angle configurations where the normal force P decreases and increases, respectively, during the incipient shearing. These results lead us to conclude that there is a tilt effect on the area reduction decay α_A , both in function of A_0 and ϕ . Here again, the quadratic law does not fit well (lower R-square) with the data of small normal forces. [Show the R-square](#). Motivated by these findings, the contact area reduction was investigate using

the power-law equation $A = A_0 - \alpha_B Q_{cn}^n$, initially proposed by Papangelo et al. [32]. The exponent n was plotted in Fig. 6.14 as a function of (a) the initial contact area A_0 and (b) the tilt angle ϕ .

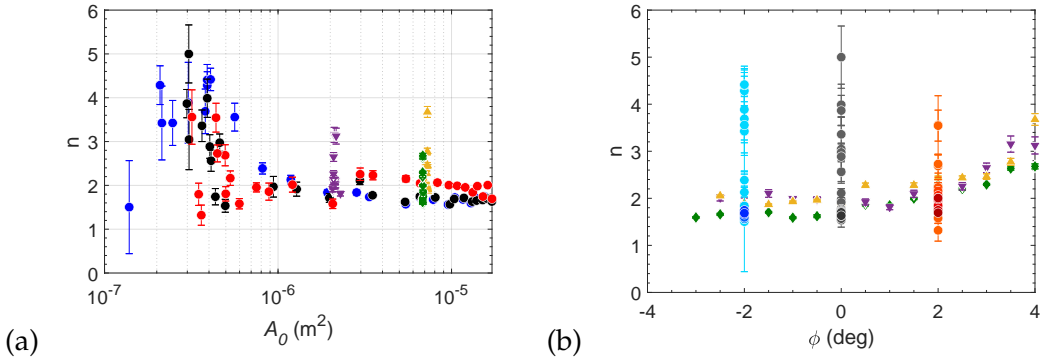


Figure 6.14: (a) Exponent n as a function of (a) the initial contact area A_0 and (b) as a function of the tilt angle ϕ . ▲ B(i): 0.78 N; ♦ B(ii): 0.78 N; ▼ B(iii): 0.10 N; and a wide range of P for ● B(iv): $\phi = -2^\circ$, ● B(iv): $\phi = 0^\circ$, and ● B(iv): $\phi = 2^\circ$. The color gradients for cases B(iv) are in function of the normal force P ; light colors for small P and dark colors for large P .

In agreement with the findings of Chapter 5 and Papangelo et al. [32], in the range of large normal load (P in the order 10^0 N) n is close to 2, and increases under small normal load. It can be seen from Fig. 6.14(b) that n also increases with the increase of the tilt angle ϕ .

6.4 Discussion

Two tilting cases were presented: case A, in which the plate (slider), the cantilever, and the tangential force sensor are tilted simultaneously; and case B, where the sphere acts as a slider and the tilt is on the plate fixed. It is worth mentioning that these are just two representative cases of many other configurations imaginable.

In both cases, we emphasize the importance of considering the forces that indeed act on the contact surface. In particular, in relation to analyses considering the normal force, as the coefficient of friction μ .

Usually, friction between two solid surfaces is characterized by μ , defined as the ratio of the peak tangential force to the corresponding normal force. Fig. 6.15 shows μ considering the unbalanced forces (filled markers) measured by the sensors, and the balanced one (open markers), after the corrections due to the presence of the tilt.

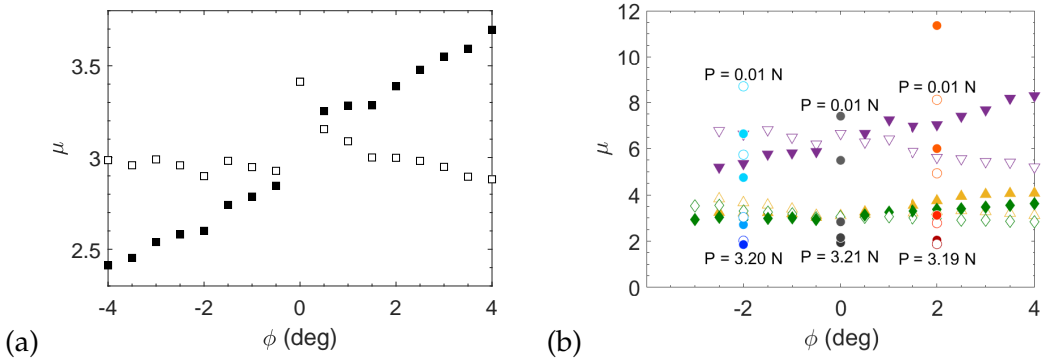


Figure 6.15: Friction coefficient μ as a function of the tilt angle ϕ for (a) case A and (b) cases B. Filled marks are for the unbalanced forces and open marks for the balanced ones. \blacktriangle B(i): 0.78 N; \blacklozenge B(ii): 0.78 N; \blacktriangledown B(iii): 0.10 N; and a wide range of P for \bullet B(iv): $\phi = -2^\circ$, \bullet B(iv): $\phi = 0^\circ$, and \bullet B(iv): $\phi = 2^\circ$. The color gradients for cases B(iv) are in function of the normal force P ; light colors for small P and dark colors for large P .

For case A shown in Fig. 6.15(a), it can be seen that the coefficients of friction μ change linearly with the increase of the tilt angle (filled markers). However, when considering the balanced force (open markers), the same value of μ is found. In fact, the force acting on the contact does not change with the angle, and this tilting configuration does not cause a variation in the contact normal force at the onset of shearing.

Recall the prob on the first 3.

In Fig. 6.15(b), for cases B, we can observe the opposite situation. Such tilt configuration makes possible a variation of normal force during the incipient shearing.

This shows us that such a simple and direct coefficient of friction calculation is very sensitive to a small misalignment between the... that can lead to incorrect conclusions, such as the non-influence of the normal force on μ .

Talk about the case B: the variation of the normal force is responsible for part of the reduction of the contact area. How to define a friction coefficient when the normal force is not constant? case B

3: the important is to look at P_{cn} and Q_{cn}

6.4.1 Contribution of normal force variation in the contact area evolution

As in cases B, there is actually a change in the contact normal force P_{cn} , this variation is responsible for part of the reduction of the contact area. In this area reduction there is a part due to the force tangential and one due to the normal force. The contact state,

which is characterized by A , depends on the forces that are independent, since they have been balanced due to the angle contribution.

In order to analyze how this variation in the normal force affects the evolution of the contact area A , two contributions to the quadratic quadratic-law equation $A = A_0 - \alpha_A Q_{cn}^2$ [37] are proposed: an **additive** contribution and a **multiplicative** one.

Additive contribution

First, according to the Hertzian contact theory, the additional contribution of the normal force is proposed in the form,

$$A = A_0 - \alpha_{add} Q_{cn}^2 + A_0 \cdot \left(\frac{P_{cn}}{P_{cn0}}^{2/3} - 1 \right) \quad (6.5)$$

This equation was used to observe the reduction of the contact area without the influence of the normal force variation. Fig. 6.16 shows the subtraction of the contribution $A_0 \cdot \left(\frac{P}{P_0}^{2/3} - 1 \right)$ from A . We can see then, that the curves of Fig. 6.16 could be regrouped, showing a similar reduction shape. Pay attention to those curves, they are just a representation of two parameters not physically connected, *i.e.*, a fraction of the contact area with with a global tangential force.

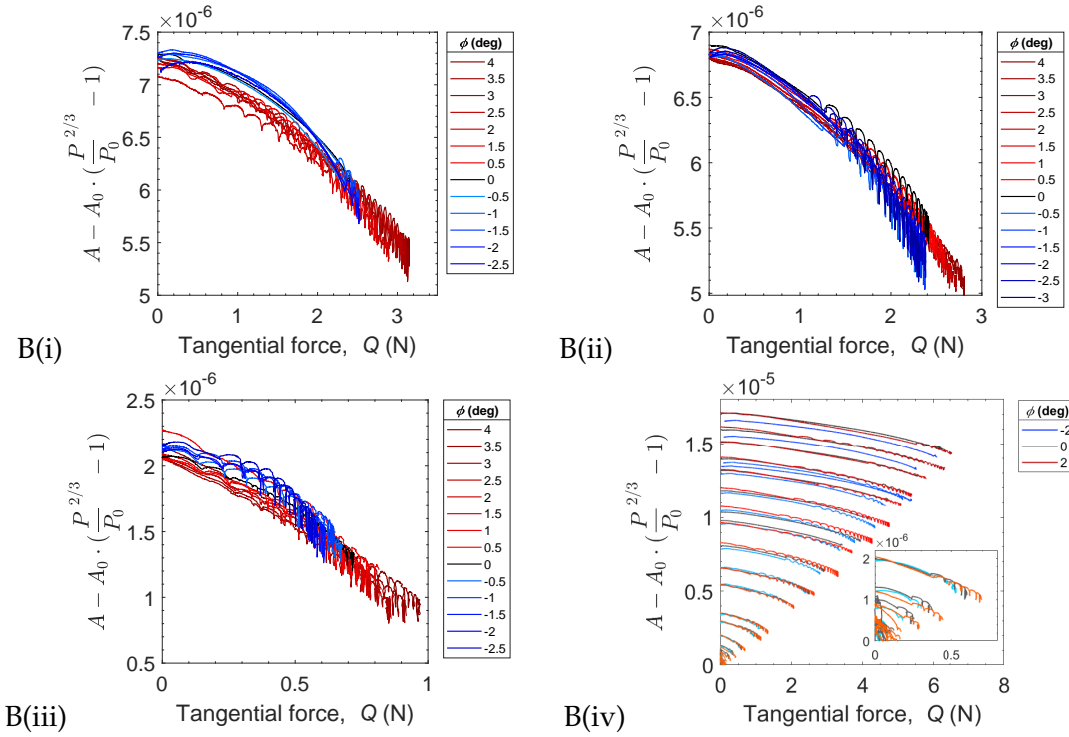


Figure 6.16: **Contact area as a function of tangential force.** B(i) $P = 0.78$ N; B(ii) $P = 0.78$ N; B(iii) $P = 0.10$ N; and B(iv) wide range of P for 3 different ϕ 's (-2° : blue lines; 0° : black lines, and 2° : red lines). The color gradients for cases B(iv) are in function of the normal force P ; light colors for small P and dark colors for large P . **Change Q to Qcn on the axis**

The area reduction parameter α_{add} was then obtained from those curves, considering a reduction with Q_{cn}^2 , and is shown in 6.17 as a function of the initial contact area A_0 and (b) as a function of the tilt angle ϕ .

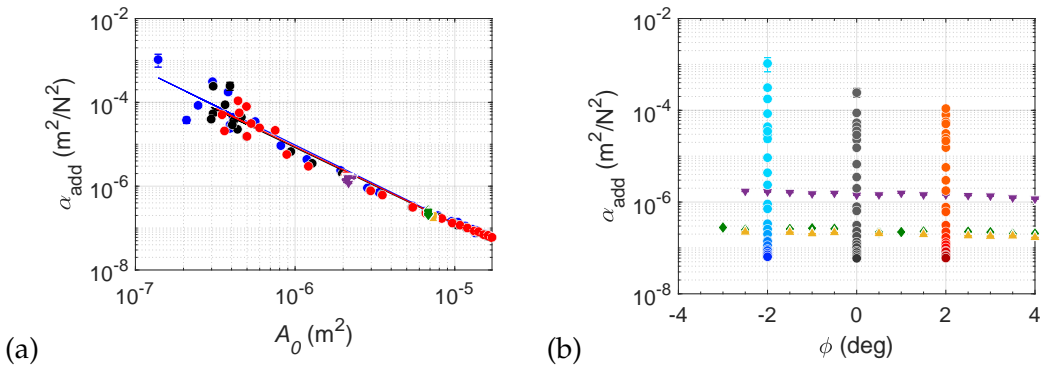


Figure 6.17: (a) **Area reduction parameter (Fit Additive Hertz) α_{add}** as a function of the initial contact area A_0 and (b) as a function of the tilt angle ϕ . Cases: \blacktriangle B(i); \blacklozenge B(ii); \blacktriangledown B(iii); 0.10 N; and a wide range of P for \bullet B(iv): $\phi = -2^\circ$, \bullet B(iv): $\phi = 0^\circ$, and \bullet B(iv): $\phi = 2^\circ$. The color gradients for cases B(iv) are in function of the normal force P ; light colors for small P and dark colors for large P .

We can see that the points are regrouped on a main curve, *i.e.*, the dependence of the angle practically disappears. This means that the effect we observed was indeed a

contribution to the variation of the normal force.

An area decrease as Q_{cn}^n [32] was also considered, since the small forces seem not to be reduced according to Q_{cn}^2 . The exponent n is, then plotted in Fig. 6.18 as a function of A_0 and ϕ . From this, we can identify a slight decrease that is just linked to the variation of the normal force during the test.

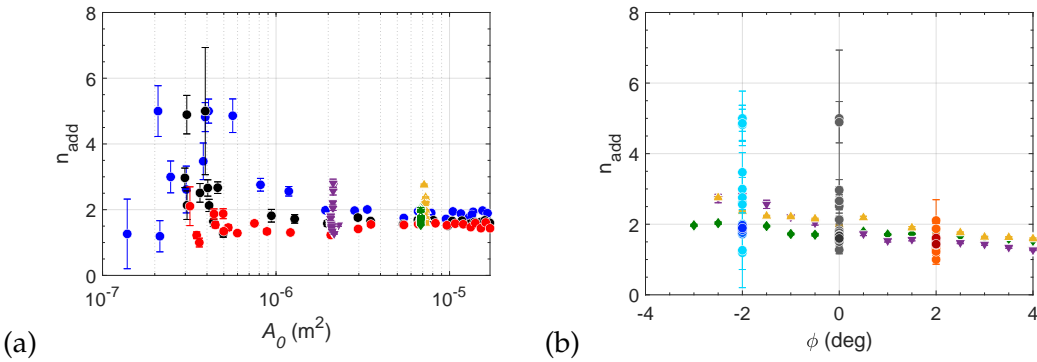


Figure 6.18: Area reduction parameter (Fit Additive) α_{add} as a function of the tilt angle ϕ . Cases: ▲ B(i): 0.78 N; ♦ B(ii): 0.78 N; ▼ B(iii): 0.10 N; and a wide range of P for ● B(iv): $\phi = -2^\circ$, ● B(iv): $\phi = 0^\circ$, and ● B(iv): $\phi = 2^\circ$. The color gradients for cases B(iv) are in function of the normal force P ; light colors for small P and dark colors for large P .

Second, the additional contribution of the normal force is proposed according to JKR contact theory,

$$A = A_0 - \alpha Q_{cn}^2 + A_0 \cdot \left[\left(\frac{P_{cn} + 6w_0\pi R + \sqrt{12w_0\pi R P_{cn} + (6w_0\pi R)^2}}{P_{cn0} + 6w_0\pi R + \sqrt{12w_0\pi R P_{cn0} + (6w_0\pi R)^2}} \right)^{2/3} - 1 \right] \quad (6.6)$$

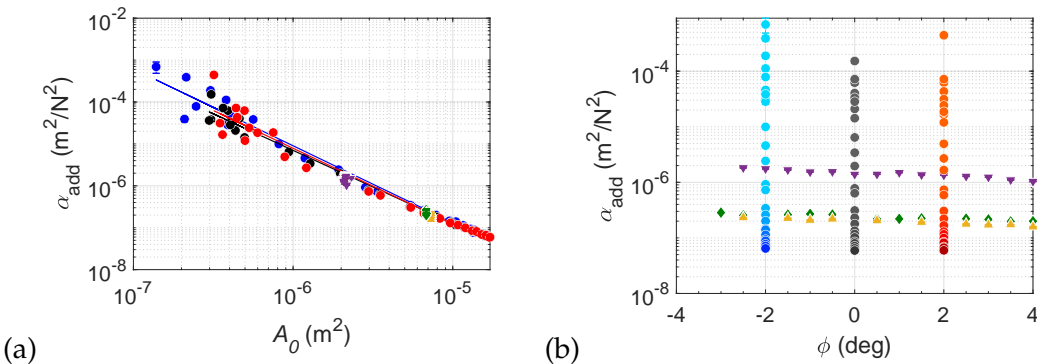


Figure 6.19: (a) Area reduction parameter (Fit Additive JKR) α_{add} as a function of the initial contact area A_0 and (b) as a function of the tilt angle ϕ . Cases: ▲ B(i): 0.78 N; ♦ B(ii): 0.78 N; ▼ B(iii): 0.10 N; and a wide range of P for ● B(iv): $\phi = -2^\circ$, ● B(iv): $\phi = 0^\circ$, and ● B(iv): $\phi = 2^\circ$. The color gradients for cases B(iv) are in function of the normal force P ; light colors for small P and dark colors for large P .

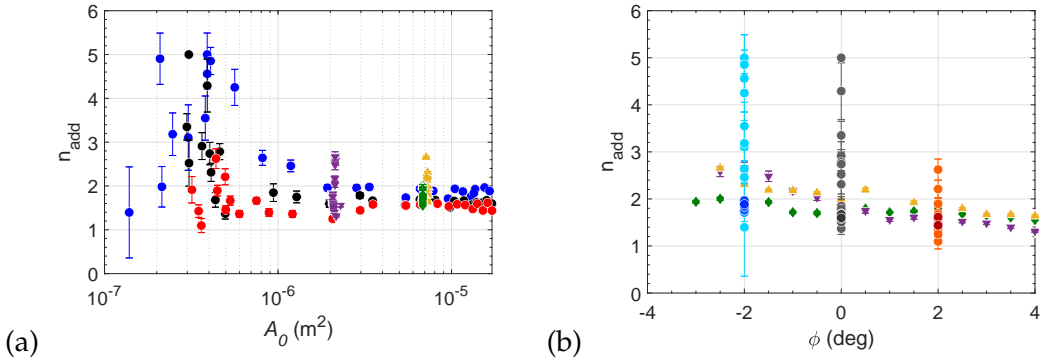


Figure 6.20: Area reduction parameter (Fit Additive JKR) α_{add} as a function of the tilt angle ϕ . Cases: ▲ B(i): 0.78 N; ♦ B(ii): 0.78 N; ▼ B(iii): 0.10 N; and a wide range of P for ● B(iv): $\phi = -2^\circ$, ● B(iv): $\phi = 0^\circ$, and ● B(iv): $\phi = 2^\circ$. The color gradients for cases B(iv) are in function of the normal force P ; light colors for small P and dark colors for large P .

Multiplicative contribution

A multiplicative contribution was also proposed according to the Hertzian contact theory in the form,

$$A = (A_0 - \alpha_{multi} Q_{cn}^2) \cdot \frac{P_{cn}}{P_{cn0}}^{2/3} \quad (6.7)$$

$$\alpha(m^2/N^{(1/3)}) (?)$$

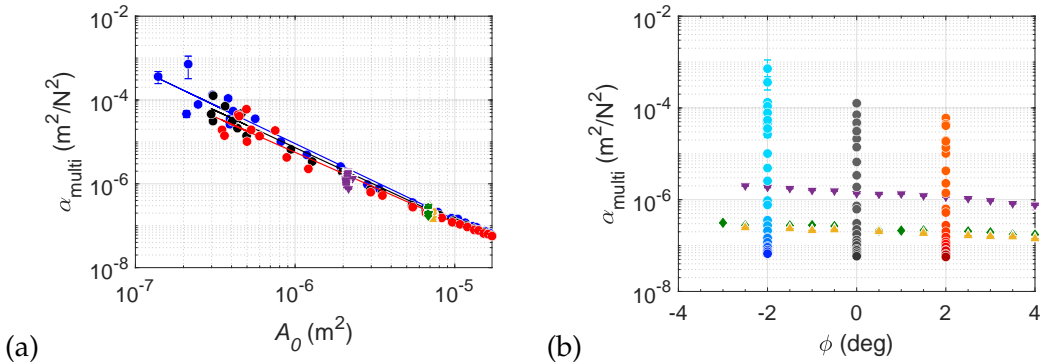


Figure 6.21: Area reduction parameter (Fit Multipliutive JKR) α_{multi} as a function of the tilt angle ϕ . Cases: ▲ B(i): 0.78 N; ♦ B(ii): 0.78 N; ▼ B(iii): 0.10 N; and a wide range of P for ● B(iv): $\phi = -2^\circ$, ● B(iv): $\phi = 0^\circ$, and ● B(iv): $\phi = 2^\circ$. The color gradients for cases B(iv) are in function of the normal force P ; light colors for small P and dark colors for large P .

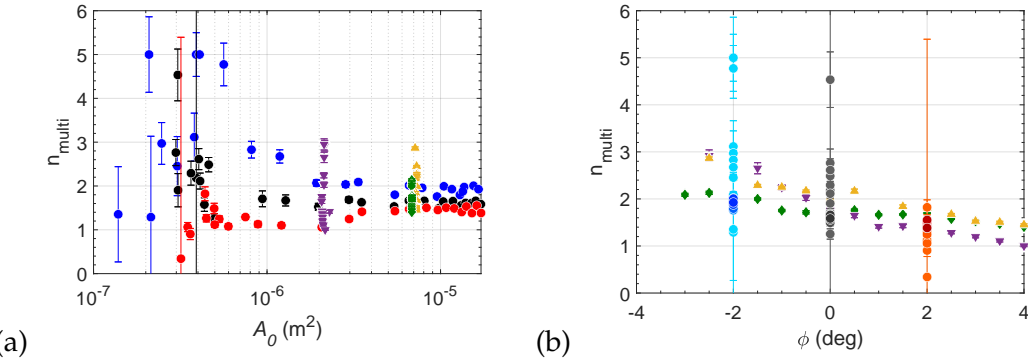


Figure 6.22: Area reduction parameter (Fit Multiplicative Hertz) α_{add} as a function of the tilt angle ϕ . Cases: \blacktriangle B(i): 0.78 N; \blacklozenge B(ii): 0.78 N; \blacktriangledown B(iii): 0.10 N; and a wide range of P for \bullet B(iv): $\phi = -2^\circ$, \bullet B(iv): $\phi = 0^\circ$, and \bullet B(iv): $\phi = 2^\circ$. The color gradients for cases B(iv) are in function of the normal force P ; light colors for small P and dark colors for large P .

Two contributions of the normal force variation to the reduction of the contact area have been proposed: an additive, considering Hertz and JKR's theory, and a multiplicative using Hertz. Fitting the experimental data we could observe the same trend in all proposition contributions, a regrouping of the rate of area reduction α on a main curve, being the proposition using Hertz's theory the best to eliminate the contribution to the normal force variation.

Considering the reduction of the contact area with Q_{cn}^n , we notice that the morphology of the reduction curve of A remains somewhat different. Which leads us to conclude that ϕ has still a certain effect on the contact area evolution.

In a qualitative analysis of the images, superimposing frames of the initial contact area (at $Q = 0$) and frames at the contact tangential force peak (at Q_{cns}), for $\phi = 0^\circ$, and the extreme angles tested (-4° and 4°), shown in Fig 6.23,

Change the Fig. below:

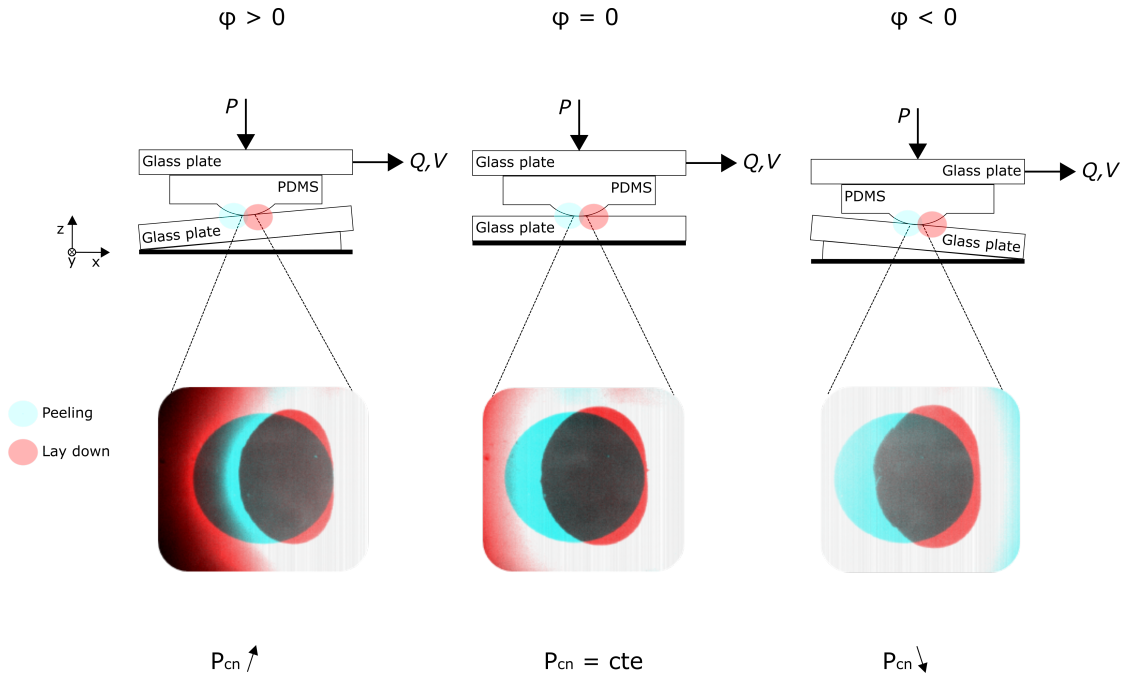


Figure 6.23: Superimposed images of the initial contact area (at $Q = 0$) and images at the static friction peak (at Q_{cns}) for $\phi = -4^\circ$ (a), 0° (b), and 4° (c). The leading edge of the contacts is on the left side. The black region is the contact area presents during the onset of sliding; the blue region the area presents at $Q = 0$ and not at Q_s ; and the red region the area not presents at $Q = 0$ but presents at Q_s .

Although we can only investigate the origin of this effect with the introduction of particles, as in Chapter 4, it can be suggest that ϕ affects the contribution of the mechanisms of the contact area reduction.

6.4.2 Shear strength

Here, the interface shear strength σ was determined and it is shown in Fig. 6.24. The endpoints of Fig. 5.10 were fitted linearly passing through the origin ($A_s = aQ_s$). Therefore, sigma is the inverse of the angular coefficient, $\sigma = 1/a$.

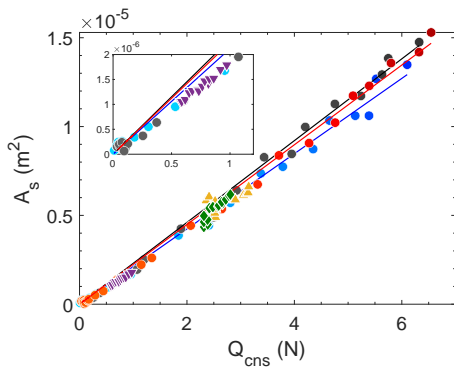


Figure 6.24: Fit σ

It can be seen that there is maybe an effect on σ . The instantaneous σ_{inst} , i.e., $\sigma_{inst} = Q_{cns}/A_s$ is also shown in Fig. 6.25 as a function of (a) ϕ and (b) Q_{cns} .

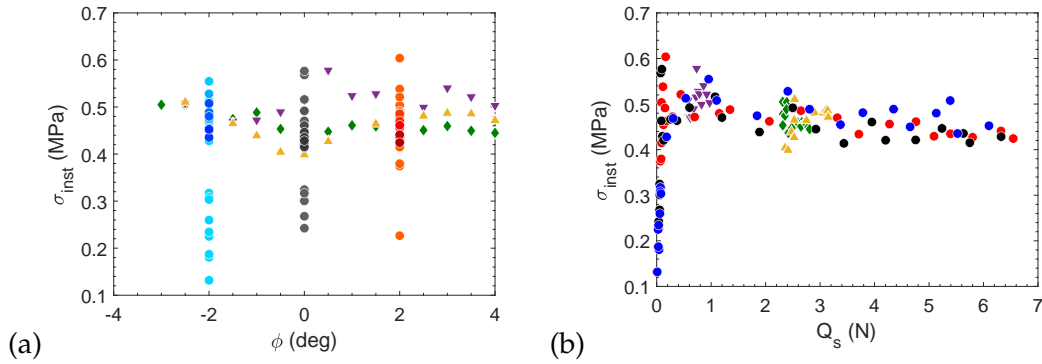


Figure 6.25: Instantaneous sigma ($\sigma_{inst} = Q_{cns}/A_s$)

We did not observe a major effect on sigma, it can be however point out a slight increase in sigma with the presence of ϕ (negative and positive).

6.5 Conclusion

Shear-induced area reduction depends on Q and P

The alignment must be made at the contact level or corrected, however it is difficult to know the angle.

we can only investigate the origin of this effect with the introduction of particles